Stable and Reproducible 2D/3D Formamidinium–Lead–Iodide Perovskite Solar Cells

Abhishek Thote[1‡], Il Jeon*[1‡], Jin-Wook Lee[2], Seungju Seo[1], Hao-Sheng Lin[1], Yang Yang[2], Hirofumi Daiguji*[1], Shigeo Maruyama*[1,3], and Yutaka Matsuo*[1]

[1]Department of Mechanical Engineering, School of Engineering, The University of Tokyo, Tokyo 113-8656, Japan

[2]Department of Materials Science and Engineering and California Nano Systems Institute, University of California, Los Angeles, CA 90095, United States

[3]Energy Nano Engineering Laboratory, National Institute of Advanced Industrial Science and Technology (AIST), Ibaraki 305-8564, Japan

*Corresponding author

I.J. E-mail: il.jeon@spc.oxon.org

H.D. E-mail: daiguji@thml.t.u-tokyo.ac.jp

S.M. E-mail: maruyama@photon.t.u-tokyo.ac.jp

Y.M. E-mail: matsuo@photon.t.u-tokyo.ac.jp

KEYWORDS : perovskite solar cell, 2D perovskite, formamidinium perovskite, mechanical property of perovskite, phase stability

ABSTRACT

2D perovskite-stabilized FACsPbI₃ (FA = Formamidinium) perovskite solar cells were fabricated in both normal-type and inverted-type architectures. While the normal-type devices exhibited a high power conversion efficiency of 20.2%, their reproducibility was limited. On the other hand, the inverted-type devices exhibited an efficiency of 18.2% with a greater stability and higher reproducibility than those of the normal-type devices. The reduced reproducibility of the normal-type devices was associated with the crack formation on the perovskite films during a spin-coating process. The hardness of both the perovskite and the sublayer was directly linked to the crack formation. Inverted-type 2D/3D FACsPbI₃ with ozone-treated poly(triarylamine) as sublayer exhibited highest phase stability owning to the hydrophobic nature of poly(triarylamine) and improved energy level alignment upon an ozone-treatment. In addition, strong interaction between phenethylamine cations of the 2D perovskite and of the 3D FACsPbI₃ crystal at grain boundaries contributed to the high phase stability.

INTRODUCTION

Organic–inorganic lead halide perovskite solar cells (PSCs) have attracted great attention owing to high absorption coefficient, low fabrication cost, and flexible applications. The high absorption arises from a suitable bandgap of perovskite materials, which is close to the Shockley–Queisser limit of 1.4 eV.[1] The bandgap of perovskite materials can also be tuned by substituting either cations and anions.[2–4] Substitution of iodide anions by a smaller halide increases the bandgaps.[4] Substitution of methylammonium (MA) cation by a bigger formamidinium (FA) cation decreases the bandgap, while retaining the cubic structure.[5–7] FA lead iodide perovskite (FAPbI₃) has been reported to possess an ideal bandgap of 1.4 eV, which corresponds to sunlight absorption up to

approximately 886 nm (**Figure S1**).[8–10] Thus, FAPbI$_3$ is potentially more suitable as an active material than MAPbI$_3$ for PSCs. However, pure FAPbI$_3$ has been reported to exhibit low stability because its trigonal α-phase is sensitive to humidity,[11] and readily turns into a nonphotoactive hexagonal δ-phase at room temperature.[12,13] Although more thermally and structurally stable FAPbI$_3$ has been realized through partial substitution of FA by Cs (FACsPbI$_3$),[14–16] the stability should be improved further to surpass MAPbI$_3$. Recently, 2D perovskite-added FACsPbI$_3$ (2D/3D FACsPbI$_3$), in which the quasi-structured 2D perovskite[17,18] protecting the 3D perovskite grains from humidity, was reported;[19] the 2D/3D FACsPbI$_3$-based PSCs in a normal-type structure gave a certified (PCE) efficiency of 19.8% with a remarkable stability.

Even though normal-type PSCs give higher PCE inverted-type PSCs have also attracted scientists.[20,21] This is because inverted-type PSCs do not require metal oxide electron-transporting layers (ETLs), which translate to a wider selection of flexible substrates,[22] devices with reduced hysteresis,[23] and improved device stability under UV illumination[24]. Thus far, there have been only a few reports on FAPbI$_3$–based inverted-type PSCs; Yuan *et al.*[25] demonstrated FAPbI$_3$–based inverted-type PSCs with a PCE of 13.6%. Han and colleagues[26–28] demonstrated higher PCEs, but with the use of a small amount of MA compounds, which led to a higher bandgap than the ideal bandgap of FA-based PSCs. Herein, we demonstrate inverted-type 2D/3D FACsPbI$_3$ PSCs and show that the devices exhibit higher reproducibility and stability than the normal-type devices. The strain caused by both 2D perovskites at grain boundaries and the big size of FA led to 2D/3D FACsPbI$_3$ being liable to form cracks.[29] However, the inverted-type 2D/3D FACsPbI$_3$ PSCs did not manifest such a problem owing to the mechanically elastic nature of the poly(triarylamine) (PTAA) sublayer, onto which the brittle 2D/3D FACsPbI$_3$ film was formed, compared with the brittle SnO$_2$ sublayer of the normal-type PSCs. The higher stability of the inverted devices came

from the reduced trap-charge,[30,31] hydrophobicity of (PTAA),[32] and exclusion of 2,2',7,7'-tetrakis[*N*,*N*-di(4-methoxyphenyl)amino]-9,9'-spirobifluorene (spiro-MeOTAD)[33]. In addition, we discovered that the strong hydrogen bonding interaction of phenethylamine (PEA) cations of the 2D perovskite with the adjacent 3D perovskite is the key to preventing the degradation by the phase change as well as by ion migration.

METHODS

Synthesis of Perovskite. A 2D/3D $FACsPbI_3$ solution is prepared using a mixture of FAI (163.0 mg, TCI), CsI (5.0 mg, TCI), PEAI (8.2 mg, TCI), PbI_2 (453.4 mg, TCI), and *N*-Methyl-2-pyrrolidone (NMP) (97.4 mg, Sigma Aldrich), mixed in 560 mg DMF (Sigma Aldrich). A 3D $FACsPbI_3$ solution is prepared using a 0.97:0.03:1 molar mixture of FAI (154.8 mg, TCI), CsI (12 mg, TCI), PbI_2 (461 mg, TCI), and NMP (97.4 mg, Sigma Aldrich), mixed in 560 mg DMF (Sigma Aldrich). A bare $FAPbI_3$ perovskite solution is prepared using a 1:1:1 molar mixture of FAI (172 mg, TCI), PbI_2 (461 mg, TCI), and NMP (97.4 mg, Sigma Aldrich), mixed in 560 mg DMF (Sigma Aldrich). A 2D PEA_2PbI_4 perovskite solution is prepared using a 2:1 molar mixture of PEAI (24.9 mg, TCI) and PbI_2 (23.0 mg, TCI), mixed in 950 mg DMF (Sigma Aldrich). All FA-based perovskite mixtures were stirred without heating, filtered using 0.02 µm, and pre-heated at 95 °C before spin-coating.

Material Characterizations. Optical microscopy, Olympus BX51, was used to analyze the presence of cracks of perovskite layers. 10x, 20x, and 50x lenses were used to observe the cracks using the Stream Start software. The surface morphology and the cracks on perovskite were analyzed by SEM using S-4800 (Hitachi). Shimadzu UV-3150 was used for the UV–vis–NIR

measurement. The surface roughness of charge carrier layers was obtained using atomic force microscopy (AFM) operating in tapping mode (SPI3800N, SII). The water contact angle measurements were performed using a contact angle meter (DMo-501, Kyowa Interface Science Co., Ltd.). The substrates were annealed on a hot plate at 110 °C for 10 min before performing the water contact angle measurements to evaporate the vapor deposited on the films. The nano-indentation tests were performed at room temperature with an indenter aligned normally using Elionix ENT-NEXUS. Mechanical properties were deduced from the load-displacement curves generated. The valence band and Fermi levels measurements of the perovskite and charge carrier layers were performed using Riken Keiki PYS-A AC-2 and Kelvin probe spectroscopy in air (ESA), respectively. The PL quenching measurements were performed using a JASCO spectrofluorometer (FP-8300). The out-of-plane X-ray diffraction tests were carried out on a Rigaku Smartlab diffractometer using Cu-Kα radiation operating with a power of 9 kW (45 kV, 200 mA). The diffraction pattern of each sample was recorded between an angular 2θ of 3º and 50º. A Raman microscope with a ×50 lens and 5×10^{-6}% of 200 mW power (Renishaw InVia with 532 nm excitation) was used. The photoemission measurements of the perovskite and charge carrier layers were performed using XPS (PHI5000, Versa Probe) with monochromatic Al Kα radiation. The XPS analysis was conducted at ultrahigh vacuum at pressures below 10^{-9} mbar.

Device fabrication. Indium-doped ITO glass substrates were cleaned with successive sonication in a detergent, deionized (DI) water, acetone, and 2-propanol baths for 15 min. The cleaned substrates were treated with UV-ozone for enhanced wettability. For reference inverted devices, PEDOT:PSS was spin-coated at 3000 rpm for 45 s as an HTL. For inverted devices with PTAA as an HTL, a 4 mg ml^{-1} solution of PTAA (Sigma Aldrich) was prepared by dissolving 2 mg of PTAA in 500 μl of toluene. The mixture was prepared inside the glove box, stirred without heating, left

for complete dissolution, and filtered using a 0.02 μm syringe filter before the use. For best-performing devices, the PTAA solution was spin-coated at 5000 rpm for 30 s, annealed at 110 for 10 min, and subjected to UV/O$_3$ treatment for 3 min. The 2D/3D FACsPbI$_3$ perovskite layer was prepared by the adduct approach. The 2D/3D FACsPbI$_3$ perovskite solution was spin-coated at 5000 rpm for 20 s, to which 0.15 mL of diethyl ether (anhydrous, >99.0%, contains BHT as stabilizer, Sigma-Aldrich) was dropped after 10 s. The resulting transparent adduct film was heat-treated at 100 °C for 1 min followed by 150 °C for 10 min. A thin layer of PC$_{61}$BM (2mg ml^{-1} in 1,2-dichlorobenzene) was spin-coated on perovskite layer at 5000 rpm for 30 s. A total 30 nm of C$_{60}$ was deposited on PC$_{61}$BM at 0.3 Å/s via thermal evaporation in vacuum. The device fabrication was completed with thermal evaporation of bathocuproine (BCP) (8 nm) and silver electrodes (70 nm). For normal reference devices, a 30 mM SnCl$_2$·2H$_2$O (Aldrich, >99.995%) solution was prepared in ethanol (anhydrous, Decon Laboratories Inc.) as a precursor solution for deposition of a compact SnO$_2$ layer. The solution was filtered by a 0.2 μm syringe filter, followed by spin-coating on the cleaned substrate at 3000 rpm for 30 s. The spin-coated film was annealed at 150 °C for 30 min. After cooling down to the room temperature, another cycle of the spin-coating process was performed, which was followed by annealing at 150 °C for 5 min and 180 °C for 1 h. SnO$_2$-coated ITO glass was treated with UV-ozone before spin-coating of the perovskite solution. A 2D/3D FACsPbI$_3$ perovskite layer was prepared by the adduct approach described above.[28–29] However, the best-performing devices had a perovskite solution spin-coated at 4000 rpm for 20 s, to which 0.15 mL of diethyl ether was dripped after 10 s, annealed at 100 °C for 1 min followed by 150 °C for 10 min. A spiro-MeOTAD solution was prepared by dissolving 85.8 mg of spiro-MeOTAD (Lumtec) in 1 mL of chlorobenzene (anhydrous, 99.8%, Sigma-Aldrich), which was mixed with 33.8 μl of a 4-tert-butylpyridine (96%, Aldrich) and 19.3 μl of Li-TFSI

(99.95%, Aldrich, 520 mg/mL in acetonitrile) solution. The spiro-MeOTAD solution was spin-coated on the perovskite layer at 3000 rpm for 20 s by dropping 17 μl of the solution during the spinning. For deposition of a metal electrode, an approximately 100-nm-thick silver layer was thermally evaporated at 0.5 Å/s on top of the spiro-MeOTAD layer.

Device characterizations. The *J–V* and MPPT characteristics of the devices were recorded using a Keithley 2401 source meter under simulated one sun illumination (AM 1.5G, 100 mW/cm^2) generated from Oriel Sol3A with class AAA solar simulator (Newport) under ambient conditions. The source meter was calibrated using a silicon diode (BS-520BK, Bunkokeiki). The external quantum efficiency measurement system consisted of an MLS-1510 monochromator to scan the UV−vis spectrum.

RESULTS AND DISCUSSION

We fabricated 2D/3D FACsPbI$_3$ PSCs using a composition of [(PEA)$_2$PbI$_4$]$_1$[FA$_{0.97}$Cs$_{0.03}$PbI$_3$]$_{59}$. Both the normal-type and inverted-type PSCs were fabricated (**Figure 1a**). The normal-type 2D/3D FACsPbI$_3$ PSCs using SnO$_2$ as an ETL gave a PCE of 20.2%, whereas the inverted-type 2D/3D FACsPbI$_3$ PSCs using poly(3,4-ethylenedioxythiophene) polystyrene sulfonate (PEDOT:PSS) as a hole-transporting layer (HTL) gave a PCE of 15.6%. Although the PCEs of the inverted-type PSCs were lower than those of the normal-type PSCs, the reproducibility was much higher for the inverted-type devices than that of the normal-type devices (**Figure 1b**). When the HTL of the inverted-type devices was changed from PEDOT:PSS to PTAA, a much higher PCE of 18.2% was obtained (**Figure 1c, Table 1, Figure S2**). A careful observation using optical microscopy and scanning electron microscopy (SEM) showed that the reproducibility difference between the normal-type and inverted-type devices originates from cracks on the perovskite films

(**Figure 1d**). The 2D/3D FACsPbI$_3$ films readily formed cracks after the spin-coating process, and the 2D/3D FACsPbI$_3$ films for normal-type devices were more liable to form cracks than those for the inverted-type devices. In the case of the normal-type PSCs, delicately controlled timing and drop-casting of an anti-solvent were necessary to avoid the crack formation. For the optimal inverted-type 2D/3D FACsPbI$_3$ PSCs, pre-heating the perovskite solution at a temperature of 95 °C was necessary to improve the film coverage on the hydrophobic PTAA film (**Figure 1e, Table S1 and S2**). In addition, 3 min ozone treatment of the PTAA HTL was necessary for the optimized result (**Table S3, Figure S3**). The PTAA-based inverted-type PSCs exhibited a PCE of 18.2% with a negligible hysteresis (**Figure 1f**). A constant maximum power point tracking (MPPT) value of approximately 17.5% was recorded for more than 500 s (**Figure 1g, Figure S4**).
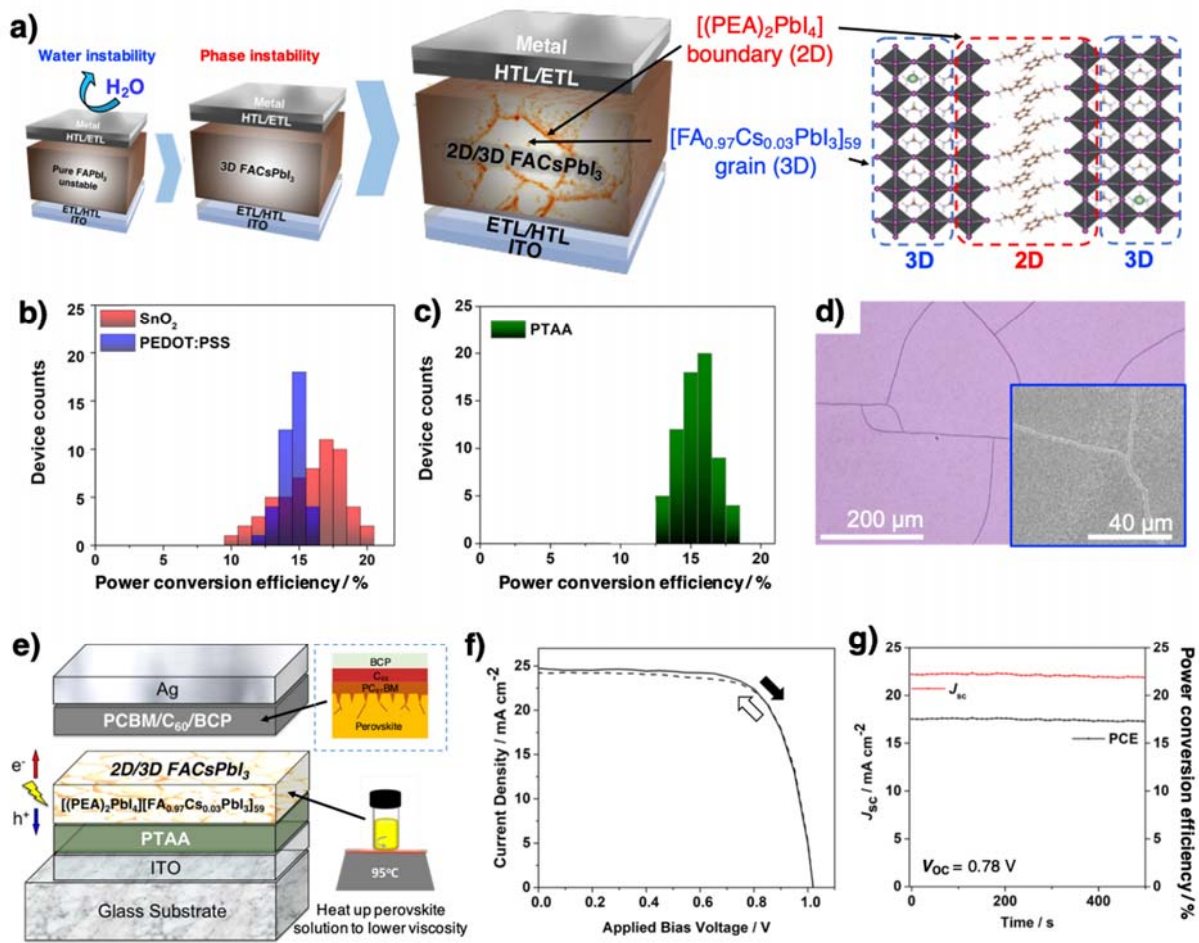
Figure 1. (a) Illustration of a 2D/3D FACsPbI₃-based PSC. (b) PCE distribution of 67 normal-type 2D/3D FACsPbI₃-based PSCs fabricated on SnO₂ (red bar) and 40 inverted-type 2D/3D FACsPbI₃-based PSCs fabricated on PEDOT:PSS. (c) PCE distribution of 76 inverted-type 2D/3D FACsPbI₃-based PSCs fabricated on PTAA. (d) Microscopic image of cracks formed on 2D/3D FACsPbI₃ films and a magnified SEM image of the same film as inset. (e) Structural schematics of a 2D/3D FACsPbI₃-based PSCs using PTAA as HTL (f) *J–V* curves under forward and reverse bias and (g) Maximum Power Point Tracking of inverted-type 2D/3D FACsPbI₃-based PSCs fabricated on PTAA.

Table 1. Photovoltaic parameters of the normal-type 2D/3D FACsPbI$_3$ PSCs on SnO$_2$ and the inverted-type 2D/3D FACsPbI$_3$ PSCs on PEDOT:PSS, PTAA, and PTAA (UV/O$_3$-treated for 3 min) under 1 sun (AM 1.5 G, 100 mW cm^{-2}).

ETL/HTL	J_{SC} (mA cm^{-2})	V_{OC} (V)	FF	R_S (Ω)	R_{SH} (Ω)	PCE$_{forward}$ (%)	PCE$_{total}$ (%)	Hysteresis Index
SnO$_2$	25.3	1.05	0.72	75.5	5.82 × 10^5	20.2	18.4	0.28
PEDOT:PSS	25.1	0.86	0.71	18.6	3.99 × 10^3	15.5	15.0	0.07
PTAA	23.7	1.00	0.66	30.5	2.34 × 10^4	16.0	15.7	0.04
PTAA (3 min UV/O$_3$)	24.6	1.02	0.72	21.2	9.09 × 10^3	18.2	17.7	0.06

It has been reported that films with thicknesses over their critical film thickness $h_{critical}$ result in crack formation (1).[34] Perovskite films in general have a thickness of around 500 nm, which exceeds the critical film thickness. Cracks are formed when evaporating dimethylformamide (DMF) solvent concentrates the perovskite grains into a closed packed array, causing liquid menisci at the top layer of the perovskite particles to exert compressive capillary force on the particle network (**Figure 2a**).[35,36] The film resists deformation in the transverse direction giving rise to transverse tensile stress (2).[37] If the grains are soft, they deform to close the pores, but if the grains are hard, the film cracks to release the stress. FAPbI$_3$ is reported to be theoretically stiffer (harder) than MAPbI$_3$.[29] Considering the degree of crack formation, it is clear that FACsPbI$_3$ films exhibit more cracks than MAPbI$_3$ films, and 2D/3D FACsPbI$_3$ films produce even more cracks than FACsPbI$_3$ films (**Figure S5**). We assume that 2D perovskites at the grain boundaries of 3D FACsPbI$_3$ films impose a great strain in 2D/3D FACsPbI$_3$ films. The nano-indentation test was conducted to analyze the film hardness. The indentation hardness (S1), elastic modulus (S2), and Martens hardness (S3) were derived from the load-displacement curves (**Figure S6, Figure S7,**

Figure S8, Figure 2b and c).[38] The test results reveal that the 2D/3D FACsPbI$_3$ films are expectedly harder than the FACsPbI$_3$ films and the MAPbI$_3$ films (**Figure 2b, Figure S8a, c, and e**). Since the 2D/3D FACsPbI$_3$ crystals are intrinsically hard, they resort to forming cracks. However, this can be alleviated if the sublayers, onto which the perovskite solution is drop-casted, are soft enough to release the transverse stress at the interface (**Figure 2a**). The crack formation can be intensified further during the annealing and cooling steps of the perovskite film fabrication. This is because of the tensile stress caused by the thermal expansion coefficient mismatch between the perovskite films and the sublayers beneath them. The nano-indentation test results of the sublayers show that metal oxide SnO$_2$ is much stiffer (harder) than PEDOT:PSS and PTAA, both of which are organic polymers (**Figure 2c, Figure S8b, d, and f**). PTAA was measured to be slightly harder than PEDOT:PSS, which explains a slight reduction in reproducibility of PTAA-based devices compared to PEDOT:PSS (**Figure 1b and c, Figure S5**). The results indicate that the mechanical properties of both the sublayer and the perovskite film are directly related to the crack formation, thus the device reproducibility.[39] Wettability (**Figure S9**) and roughness (**Figure S10**) of the sublayers did not affect the crack formation of the films.

$$h_{critical} \sim \gamma \frac{G^{1/2}}{(-P_{\max})^{3/2}} \qquad (1)$$
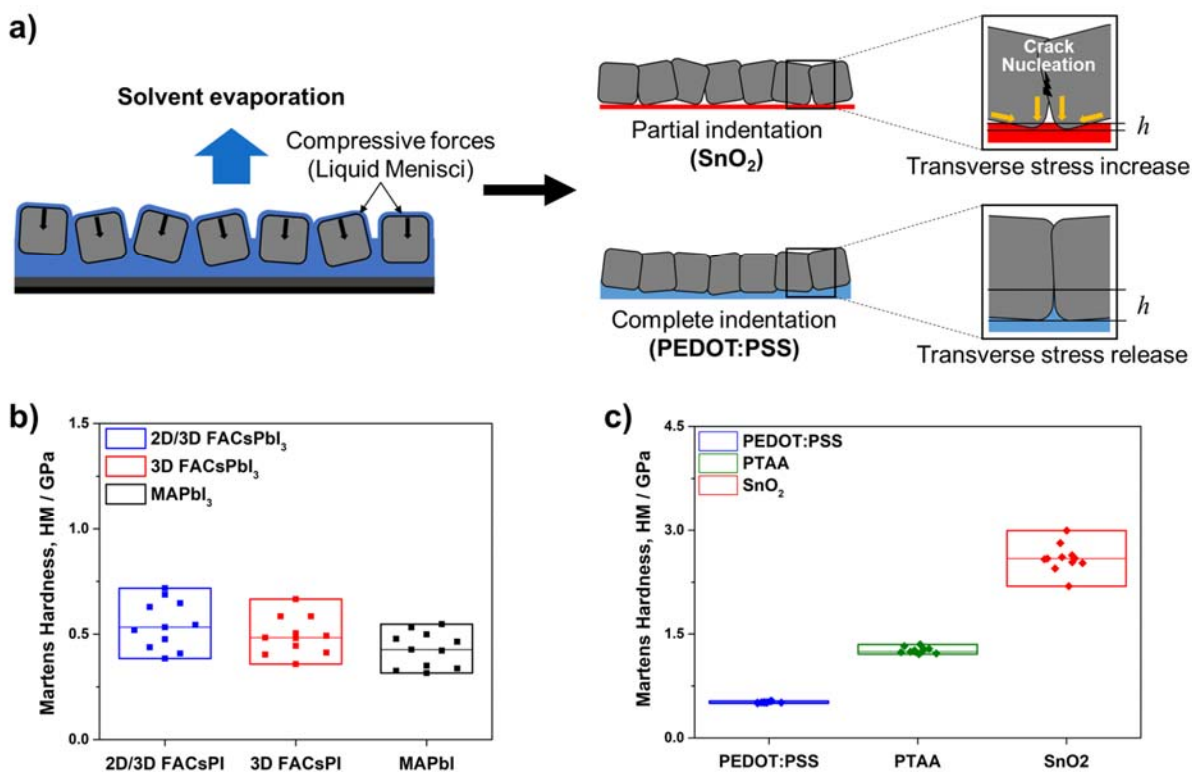
$$\sigma = G\varepsilon^2 \qquad (2)$$

Figure 2. (a) Illustration of crack formation in perovskite films on SnO$_2$ (upper, red) and PEDOT:PSS (lower, blue) with different indentation depths, *h*, indicating different transverse stresses. Martens hardness (HM) of (b) three different perovskite films (2D/3D FACsPbI$_3$, 3D FACsPbI$_3$, and MAPbI$_3$) and (c) three different sublayers (PEDOT:PSS, PTAA, and SnO$_2$).

The energy level alignment is also an important factor for the device performance. Photoelectron yield spectroscopy (PYS) and the Kelvin probe measurement were used to measure the energy levels of the films used in this work (**Figure S11**). Using the obtained data, an energy level diagram is drawn in **Figure S12.** The energy level diagram shows that ozone treatment shifts the highest occupied molecular orbital (HOMO) level of PTAA down from −5.3 eV to −5.6 eV, aligning with the valence band of the 2D/3D FACsPbI$_3$ film better than before the treatment. According to the energy diagram, both PEDOT:PSS and ozone-treated PTAA exhibited better energy matching with

the 2D/3D FACsPbI$_3$ film than SnO$_2$. This is corroborated by photoluminescence (PL) data, in which both PEDOT:PSS and ozone-treated PTAA display stronger quenching of PL than SnO$_2$ (**Figure S13**). In addition, the quenched PL spectra blue-shifted with a reduced full-width half maximum, indicating more spontaneous radiative recombination and reduced shallow trap density.[40–42]
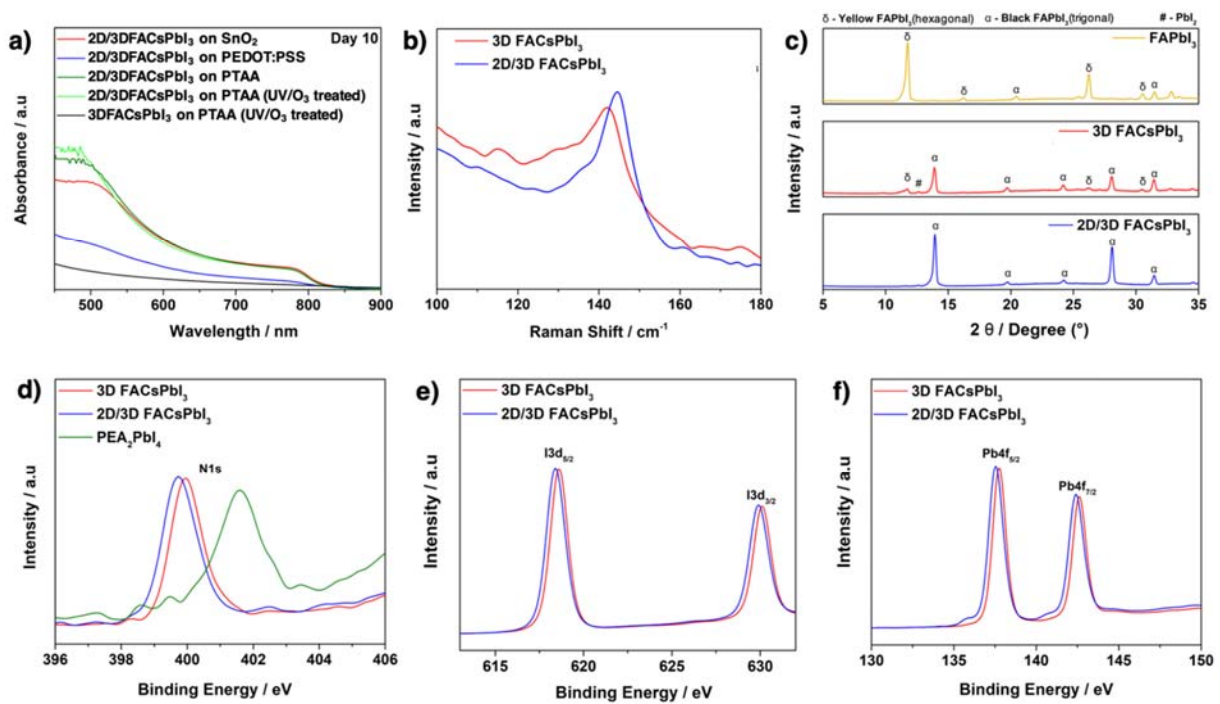

Figure 3. (a) UV-vis absorption spectra change of the perovskite films on various sublayers after 10 days in ambience (25 °C, 40% R.H). b) Raman spectra of FACsPbI$_3$ (red line) and 2D/3D FACsPbI$_3$ (blue line) after one day in ambience. c) XRD spectra of FAPbI$_3$ (yellow line), FACsPbI$_3$ (red line), and 2D/3D FACsPbI$_3$ (blue line) left in ambience for 10 days. XPS spectra of FACsPbI$_3$ (red line) and 2D/3D FACsPbI$_3$ (blue line) for d) iodine peak, e) lead peak, and f) nitrogen peak.

The perovskite films on different sublayer films were exposed to constant illumination of one sun for the stability test. Both the color change (**Figure S14**) and the UV-vis absorption spectra decrease of the perovskite films over time (**Figure 3a**, **Figure S15**) show that 2D/3D FACsPbI$_3$ on ozone-treated PTAA exhibits the highest stability among the samples. The stability of the 2D/3D FACsPbI$_3$ film on PTAA is slightly higher when the PTAA sublayer is ozone-treated. We attribute this to better energy alignment of ozone-treated PTAA, because lingering charge arising from energy misalignment induces faster degradation of perovskite films.[31] The 2D/3D FACsPbI$_3$ films on SnO$_2$ degraded even faster owing to the energy misalignment and high chemical capacitance of SnO$_2$.[30,31] The 2D/3D FACsPbI$_3$ on PEDOT:PSS degraded much faster despite a better energy alignment of PEDOT:PSS with 2D/3D FACsPbI$_3$. We ascribe this to the hygroscopic nature of PEDOT:PSS as well as its acidic nature, which can etch the tin oxide (ITO) electrodes.[43,44] 2D/3D FACsPbI$_3$ based PSCs using ozone-treated PTAA as sublayer also exhibited much higher stability than those using SnO$_2$ and PEDOT:PSS as sublayer (**Figure S16**). It is important to note that the 3D FACsPbI$_3$ films degraded much faster than the 2D/3D FACsPbI$_3$ films even on ozone-treated PTAA (**Figure 3a**, **Figure S15**). The Raman spectra of 2D/3D FACsPbI$_3$ and 3D FACsPbI$_3$ after being left in ambience for one-day show that 3D FACsPbI$_3$ contains more nonphotoactive hexagonal δ-phase than 2D/3D FACsPbI$_3$ (**Figure 3b**). The blue-shifted peak at 145.3 cm^{-1} for the 2D/3D FACsPbI$_3$ film is indicative of the in-plane vibration of trigonal α-phase FA cations.[9,45] The X-ray diffraction (XRD) patterns of the perovskite films left in ambience for 10 days clearly demonstrate the phase stability difference between 2D/3D FACsPbI$_3$ and 3D FACsPbI$_3$ (**Figure 3c**). The pure yellow phase δ-FAPbI$_3$ peaks of bare FAPbI$_3$ depict a complete phase change from α-FAPbI$_3$ to δ-FAPbI$_3$. 3D FACsPbI$_3$ retained the α-FAPbI$_3$ for 3 days, but transitioned to δ-FAPbI$_3$ phase thereafter. 2D/3D FACsPbI$_3$ demonstrates the

highest phase stability to the phase change under ambient conditions as can be seen from the peaks corresponding to pure black phase α-FAPbI$_3$. The origin of the phase stability of 2D/3D FACsPbI$_3$ was studied using X-ray photoelectron spectroscopy (XPS). All the spectra were calibrated by the C 1s peak. Since 2D PEA$_2$PbI$_4$ sits at the grain boundaries of 3D FACsPbI$_3$, it is important to analyze the interaction between PEA cations and I atoms in octahedral PbI$_6^{4-}$ using the N 1s peak. The N 1s peak of PEA$_2$PbI$_4$ is at a higher binding energy than that of 3D FACsPbI$_3$ (**Figure 3d)**. This indicates that there is hydrogen bonding between the ammonium heads (NH$^+$) of PEA to the adjacent I in PbI$_6^{4-}$ in PEA$_2$PbI$_4$ **(Figure S17)**.[46] In 2D/3D FACsPbI$_3$, the ammonium heads (NH$^+$) of PEA form hydrogen bonding with both the bridging I atoms and the terminal I atoms of PbI$_6^{4-}$ octahedra, which affect FA$^+$–I and Pb–I, respectively (**Figure S18**). The hydrogen boding influencing FA$^+$–I is evidenced by the N 1s peak of 2D/3D FACsPbI$_3$ positioned at a lower binding energy than that of 3D FACsPbI$_3$. This is because in 2D/3D FACsPbI$_3$, the bond strength of FA$^+$–I is reduced by the pull from the PEA cations at the grain boundaries (**Figure S18**). The hydrogen boding influencing Pb–I is evidenced by both the I 3d and Pb 4f peaks of 2D/3D FACsPbI$_3$ positioned at lower binding energies than those of 3D FACsPbI$_3$ (**Figure 3 e and 3f**). Such strong interactions result in the increase in the bond lengths of Pb–I (reduction in the bond strength). It is worth noting that there are small shoulders in the Pb 4f spectrum of 2D/3D FACsPbI$_3$. They correspond to Pb^0 atoms from the broken Pb–I bonds caused by strong pull of PEA cations, corroborating our hypothesis (**Figure S18**). Pb–I bonds are reported to be significantly short in δ-FAPbI$_3$ than in α-FAPbI$_3$.[47] Therefore, the phase transition from the α-FAPbI$_3$ phase to the δ-FAPbI$_3$ phase is more difficult to occur in 2D/3D FACsPbI$_3$ (**Figure S19**).[48–50] In addition to this, it is reported that the presence of PEA cations suppresses the iodide migration, which reduces hysteresis, thus improving the stability against the ion migration from the metal electrode.[48] The

combination of these characteristics explains why 2D/3D $FACsPbI_3$ shows an exceptional operational stability, particularly in the inverted structure.

CONCLUSIONS

The inverted-type 2D/3D $FACsPbI_3$ PSCs were demonstrated. It was found that the inverted-type devices exhibit higher reproducibility and stability, despite marginally lower PCEs. We conclude that the high reproducibility is linked to the mechanical properties of the perovskite films and sublayers. 2D/3D $FACsPbI_3$ was found to possess a robust phase stability, which is attributed to strong hydrogen bonding between PEA cations and the 3D $FACsPbI_3$ crystal grain surface. We are confident that this finding will provide a better understanding of the 2D/3D perovskite technology, consequently contributing to the field of solar cell research.

ASSOCIATED CONTENT

Supporting Information: *J-V* curve of inverted and normal based devices; Optimization of Perovskite solution annealing temperatures, PTAA concentration levels, ozone treatment of PTAA films; MPPT and EQE data of optimized devices; Optical microscopic analysis of cracks on Perovskite films; Nanoindentation tests; Water contact angle and AFM tests; PYS and Kelvin Probe test; PL Quenching; Film and device stability tests. The Supporting Information is available free of charge on the ACS Publications website.

AUTHOR INFORMATION

Corresponding Author

*Corresponding authors

I.J. E-mail: il.jeon@spc.oxon.org

H.D. E-mail: daiguji@thml.t.u-tokyo.ac.jp

S.M. E-mail: maruyama@photon.t.u-tokyo.ac.jp

Y.M. E-mail: matsuo@photon.t.u-tokyo.ac.jp

Author Contributions

A.T. and I.J. contributed equally to this work (indicated by ‡). I.J., H.D., S.M., and Y.M. conceived the project. A.T. and S.S. fabricated the devices. A.T., I.J., and H.L. carried out the analyses. J.L. and Y.Y. provided the 2D/3D FACsPbI$_3$ technology. I.J., H.D., and S.M. provided technical advice throughout the project. A.T., I.J., H.D., and Y.M. wrote the manuscript.

Notes

The authors declare no competing financial interest.

REFERENCES

(1)   Shockley, W.; Queisser, H. J. Detailed Balance Limit of Efficiency of p-n Junction Solar Cells. *J. Appl. Phys.* **1961**, *32*, 510–519.

(2)   Tanaka, K.; Kondo, T. Bandgap and exciton binding energies in lead-iodide-based natural quantum-well crystals. *Sci. Technol. Adv. Mater.* **2003**, *4*, 599–604.

(3)   Zhang, W.; Anaya, M.; Lozano, G.; Calvo, M. E.; Johnston, M. B.; Míguez, H.; Snaith, H. J. Highly Efficient Perovskite Solar Cells with Tunable Structural Color. *Nano Lett.* **2015**, *15*, 1698–1702.

(4)   Noh, J. H.; Im, S. H.; Heo, J. H.; Mandal, T. N.; Seok, S. Il. Chemical Management for Colorful, Efficient, and Stable Inorganic–Organic Hybrid Nanostructured Solar Cells. *Nano Lett.* **2013**, *13*, 1764–1769.

(5)   Baikie, T.; Fang, Y.; Kadro, J. M.; Schreyer, M.; Wei, F.; Mhaisalkar, S. G.; Graetzel, M.; White, T. J. Synthesis and crystal chemistry of the hybrid perovskite $(CH_3NH_3)PbI_3$ for solid-state sensitised solar cell applications. *J. Mater. Chem. A* **2013**, *1*, 5628.

(6)   Borriello, I.; Cantele, G.; Ninno, D. Ab initio investigation of hybrid organic-inorganic perovskites based on tin halides. *Phys. Rev. B* **2008**, *77*, 235214.

(7)   Pang, S.; Hu, H.; Zhang, J.; Lv, S.; Yu, Y.; Wei, F.; Qin, T.; Xu, H.; Liu, Z.; Cui, G. $NH_2CH=NH_2PbI_3$: An Alternative Organolead Iodide Perovskite Sensitizer for Mesoscopic Solar Cells. *Chem. Mater.* **2014**, *26*, 1485–1491.

(8)   Eperon, G. E.; Stranks, S. D.; Menelaou, C.; Johnston, M. B.; Herz, L. M.; Snaith, H. J. Formamidinium lead trihalide: a broadly tunable perovskite for efficient planar heterojunction solar cells. *Energy Environ. Sci.* **2014**, *7*, 982.

(9)   Han, Q.; Bae, S.-H.; Sun, P.; Hsieh, Y.-T.; Yang, Y. M.; Rim, Y. S.; Zhao, H.; Chen, Q.; Shi, W.; Li, G.; Yang, Y. Single Crystal Formamidinium Lead Iodide (FAPbI$_3$): Insight into the Structural, Optical, and Electrical Properties. *Adv. Mater.* **2016**, *28*, 2253–2258.

(10)   Jesper Jacobsson, T.; Correa-Baena, J.-P.; Pazoki, M.; Saliba, M.; Schenk, K.; Grätzel, M.; Hagfeldt, A. Exploration of the compositional space for mixed lead halogen perovskites for high efficiency solar cells. *Energy Environ. Sci.* **2016**, *9*, 1706–1724.

(11)   Jeon, N. J.; Noh, J. H.; Yang, W. S.; Kim, Y. C.; Ryu, S.; Seo, J.; Seok, S. Il. Compositional engineering of perovskite materials for high-performance solar cells. *Nature* **2015**, *517*, 476–480.

(12)   Lee, J.-W.; Seol, D.-J.; Cho, A.-N.; Park, N.-G. High-Efficiency Perovskite Solar Cells Based on the Black Polymorph of $HC(NH_2)_2PbI_3$. *Adv. Mater.* **2014**, *26*, 4991–4998.

(13)   Stoumpos, C. C.; Malliakas, C. D.; Kanatzidis, M. G. Semiconducting Tin and Lead Iodide Perovskites with Organic Cations: Phase Transitions, High Mobilities, and Near-Infrared Photoluminescent Properties. *Inorg. Chem.* **2013**, *52*, 9019–9038.

(14)   McMeekin, D. P.; Sadoughi, G.; Rehman, W.; Eperon, G. E.; Saliba, M.; Horantner, M. T.; Haghighirad, A.; Sakai, N.; Korte, L.; Rech, B.; Johnston, M. B.; Herz, L. M.; Snaith, H. J. A mixed-cation lead mixed-halide perovskite absorber for tandem solar cells. *Science* **2016**, *351*, 151–155.

(15)   Yi, C.; Luo, J.; Meloni, S.; Boziki, A.; Ashari-Astani, N.; Grätzel, C.; Zakeeruddin, S. M.;

Röthlisberger, U.; Grätzel, M. Entropic stabilization of mixed A-cation ABX$_3$ metal halide perovskites for high performance perovskite solar cells. *Energy Environ. Sci.* **2016**, *9*, 656–662.

(16)   Lee, J.-W.; Kim, D.-H.; Kim, H.-S.; Seo, S.-W.; Cho, S. M.; Park, N.-G. Formamidinium and Cesium Hybridization for Photo- and Moisture-Stable Perovskite Solar Cell. *Adv. Energy Mater.* **2015**, *5*, 1501310.

(17)   Byun, J.; Cho, H.; Wolf, C.; Jang, M.; Sadhanala, A.; Friend, R.H.; Yang, H.; Lee, T-W. Efficient Visible Quasi-2D Perovskite Light-Emitting Diodes. *Adv.Mater.* **2016**, *28*, 7515–7520.

(18)   Yan, J.; Qiu, W.; Wu, G.; Heremans, P.; Chen, H. Recent progress in 2D/quasi-2D layered metal halide perovskites for solar cells. *J. Mater. Chem. A*, **2018**, *6*, 11063.

(19)   Lee, J.-W.; Dai, Z.; Han, T.-H.; Choi, C.; Chang, S.-Y.; Lee, S.-J.; Marco, N De.; Zhao, H.; Sun, P.; Huang, Y.; Yang, Y. 2D perovskite stabilized phase-pure formamidinium perovskite solar cells. *Nat. Commun.* **2017**, *8*, 15684.

(20)   Kim, H.; Lim, K-G.; Lee T-W. Planar heterojunction organometal halide perovskite solar cells: roles of interfacial layers. *Energy Environ. Sci.*, **2016**,*9*, 12-30.

(21)   Heo, J.H.; Song, D.H.; Han, H.J.; Kim, S.Y.; Kim, J.H.; Kim, D.; Shin, H.W.; Ahn, T.K.; Wolf, C.; Lee, T-W.; Im, S.H. Planar CH$_3$NH$_3$PbI$_3$ Perovskite Solar Cells with Constant 17.2% Average Power Conversion Efficiency Irrespective of the Scan Rate. *Adv.Mater.*, **2015**, *27*, 3424–3430.

(22)   Li, Y.; Meng, L.; Yang, Y. (Michael); Xu, G.; Hong, Z.; Chen, Q.; You, J.; Li, G.; Yang, Y.; Li, Y. High-efficiency robust perovskite solar cells on ultrathin flexible substrates. *Nat. Commun.* **2016**, *7*, 10214.

(23)   Jeon, I.; Yoon, J.; Ahn, N.; Atwa, M.; Delacou, C.; Anisimov, A.; Kauppinen, E. I.; Choi, M.; Maruyama, S.; Matsuo, Y. Carbon Nanotubes versus Graphene as Flexible Transparent Electrodes in Inverted Perovskite Solar Cells. *J. Phys. Chem. Lett.* **2017**, *8*, 5395–5401.

(24)   Leijtens, T.; Eperon, G. E.; Pathak, S.; Abate, A.; Lee, M. M.; Snaith, H. J. Overcoming ultraviolet light instability of sensitized TiO$_2$ with meso-superstructured organometal tri-halide perovskite solar cells. *Nat. Commun.* **2013**, *4*, 2885.

(25)   Yuan, D.-X.; Gorka, A.; Xu, M.-F.; Wang, Z.-K.; Liao, L.-S. Inverted planar NH$_2$CH═NH$_2$PbI$_3$ perovskite solar cells with 13.56% efficiency via low temperature processing. *Phys. Chem. Chem. Phys.* **2015**, *17*, 19745–19750.

(26)   Wu, Y.; Yang, X.; Chen, W.; Yue, Y.; Cai, M.; Xie, F.; Bi, E.; Islam, A.; Han, L. Perovskite solar cells with 18.21% efficiency and area over 1 cm^2 fabricated by heterojunction engineering. *Nat. Energy* **2016**, *1*, 16148.

(27)   Liu, J.; Shirai, Y.; Yang, X.; Yue, Y.; Chen, W.; Wu, Y.; Islam, A.; Han, L. High-Quality

Mixed-Organic-Cation Perovskites from a Phase-Pure Non-stoichiometric Intermediate (FAI)$_{1-x}$ -PbI$_2$ for Solar Cells. *Adv. Mater.* **2015**, *27*, 4918–4923.

(28) Xie, F.; Chen, C.; Wu, Y.; Li, X.; Cai, M.; Liu, X.; Yang, X.; Han, L. Vertical recrystallization for highly efficient and stable formamidinium-based inverted-structure perovskite solar cells. *Energy Environ. Sci.* **2017**, *10*, 1942–1949.

(29) Sun, S.; Isikgor, F. H.; Deng, Z.; Wei, F.; Kieslich, G.; Bristowe, P. D.; Ouyang, J.; Cheetham, A. K. Factors Influencing the Mechanical Properties of Formamidinium Lead Halides and Related Hybrid Perovskites. *ChemSusChem* **2017**, *10*, 3740–3745.

(30) Ahn, N.; Jeon, I.; Yoon, J.; Kauppinen, E. I.; Matsuo, Y.; Maruyama, S.; Choi, M. Carbon-sandwiched perovskite solar cell. *J. Mater. Chem. A* **2018**, *6*, 1382–1389.

(31) Ahn, N.; Kwak, K.; Jang, M. S.; Yoon, H.; Lee, B. Y.; Lee, J.; Pikhitsa, P. V; Byun, J.; Choi, M. Trapped charge-driven degradation of perovskite solar cells. *Nat. Commun.* **2016**, *7*, 13422.

(32) Bi, C.; Wang, Q.; Shao, Y.; Yuan, Y.; Xiao, Z.; Huang, J. Non-wetting surface-driven high-aspect-ratio crystalline grain growth for efficient hybrid perovskite solar cells. *Nat. Commun.* **2015**, *6*, 7747.

(33) Jeon, I.; Ueno, H.; Seo, S.; Aitola, K.; Nishikubo, R.; Saeki, A.; Okada, H.; Boschloo, G.; Maruyama, S.; Matsuo, Y. Lithium-Ion Endohedral Fullerene (Li$^+$ @C60) Dopants in Stable Perovskite Solar Cells Induce Instant Doping and Anti-Oxidation. *Angew. Chemie Int. Ed.* **2018**, *57*, 4607–4611.

(34) Chiu, R. C.; Garino, T. J.; Cima, M. J. Drying of Granular Ceramic Films: I, Effect of Processing Variables on Cracking Behavior. *J. Am. Ceram. Soc.* **1993**, *76*, 2257–2264.

(35) Man, W.; Russel, W. B. Direct Measurements of Critical Stresses and Cracking in Thin Films of Colloid Dispersions. *Phys. Rev. Lett.* **2008**, *100*, 198302.

(36) Routh, A. F.; Russel, W. B. A Process Model for Latex Film Formation: Limiting Regimes for Individual Driving Forces. *Langmuir* **1999**, *15*, 7762–7773.

(37) Singh, K. B.; Tirumkudulu, M. S. Cracking in Drying Colloidal Films. *Phys. Rev. Lett.* **2007**, *98*, 218302.

(38) Shahdad, S. A.; McCabe, J. F.; Bull, S.; Rusby, S.; Wassell, R. W. Hardness measured with traditional Vickers and Martens hardness methods. *Dent. Mater.* **2007**, *23*, 1079–1085.

(39) Rolston, N.; Bush, K. A.; Printz, A. D.; Gold-Parker, A.; Ding, Y.; Toney, M. F.; McGehee, M. D.; Dauskardt, R. H. Engineering Stress in Perovskite Solar Cells to Improve Stability. *Adv. Energy Mater.* **2018**, *8*, 1802139.

(40) Xu, J.; Buin, A.; Ip, A. H.; Li, W.; Voznyy, O.; Comin, R.; Yuan, M.; Jeon, S.; Ning, Z.; McDowell, J. J.; Kanjanaboos, P.; Sun, J.-P.; Lan, X.; Quan, L. N.; Kim, D. H.; Hill, I. G.;

Maksymovych, P.; Sargent, E. H. Perovskite–fullerene hybrid materials suppress hysteresis in planar diodes. *Nat. Commun.* **2015**, *6*, 7081.

(41) de Quilettes, D. W.; Vorpahl, S. M.; Stranks, S. D.; Nagaoka, H.; Eperon, G. E.; Ziffer, M. E.; Snaith, H. J.; Ginger, D. S. Impact of microstructure on local carrier lifetime in perovskite solar cells. *Science* **2015**, *348*, 683–686.

(42) Lin, H.-S.; Jeon, I.; Xiang, R.; Seo, S.; Lee, J.-W.; Li, C.; Pal, A.; Manzhos, S.; Goorsky, M. S.; Yang, Y.; Maruyama, S.; Matsuo, Y. Achieving High Efficiency in Solution-Processed Perovskite Solar Cells Using C60/C70 Mixed Fullerenes. *ACS Appl. Mater. Interfaces* **2018**, acsami.8b11049.

(43) Jeon, I.; Delacou, C.; Okada, H.; Morse, G. E.; Han, T.-H.; Sato, Y.; Anisimov, A.; Suenaga, K.; Kauppinen, E. I.; Maruyama, S.; Matsuo, Y. Polymeric acid-doped transparent carbon nanotube electrodes for organic solar cells with the longest doping durability. *J. Mater. Chem. A* **2018**, *6*, 14553–14559.

(44) Domanski, K.; Correa-Baena, J.-P.; Mine, N.; Nazeeruddin, M. K.; Abate, A.; Saliba, M.; Tress, W.; Hagfeldt, A.; Grätzel, M. Not All That Glitters Is Gold: Metal-Migration-Induced Degradation in Perovskite Solar Cells. *ACS Nano* **2016**, *10*, 6306–6314.

(45) Steele, J. A.; Yuan, H.; Tan, C. Y. X.; Keshavarz, M.; Steuwe, C.; Roeffaers, M. B. J.; Hofkens, J. Direct Laser Writing of δ- to α-Phase Transformation in Formamidinium Lead Iodide. *ACS Nano* **2017**, *11*, 8072–8083

(46) Mitzi, D. B. Synthesis, Structure, and Properties of OrganicInorganic Perovskites and Related Materials. In Progress in Inorganic Chemistry; John Wiley & Sons, Inc.: New York, **2007**; pp 1–121.

(47) Weller, M. T.; Weber, O. J.; Frost, J. M.; Walsh, A. Cubic Perovskite Structure of Black Formamidinium Lead Iodide, α-[HC(NH$_2$)$_2$]PbI$_3$, at 298 K. *J. Phys. Chem. Lett.* **2015**, *6*, 3209–3212.

(48) Chen, J.; Lee, D.; Park, N.-G. Stabilizing the Ag Electrode and Reducing *J–V* Hysteresis through Suppression of Iodide Migration in Perovskite Solar Cells. *ACS Appl. Mater. Interfaces* **2017**, *9*, 36338–36349.

(49) Nazarenko, O.; Yakunin, S.; Morad, V.; Cherniukh, I.; Kovalenko, M. V. Single crystals of caesium formamidinium lead halide perovskites: solution growth and gamma dosimetry. *NPG Asia Mater.* **2017**, *9*, e373–e373.

(50) Liu, T.; Zong, Y.; Zhou, Y.; Yang, M.; Li, Z.; Game, O. S.; Zhu, K.; Zhu, R.; Gong, Q.; Padture, N. P. High-Performance Formamidinium-Based Perovskite Solar Cells via Microstructure-Mediated δ‑to‑α Phase Transformation. *Chem. Mater.* **2017**, *29*, 3246–3250.

2D Perovskite stabilizing α-FAPbI₃

H₂O

BCP / Ag
PC₆₁BM / C₆₀
2D/3D FACsPbI₃
PTAA
ITO

Cracks affecting Reproducibility
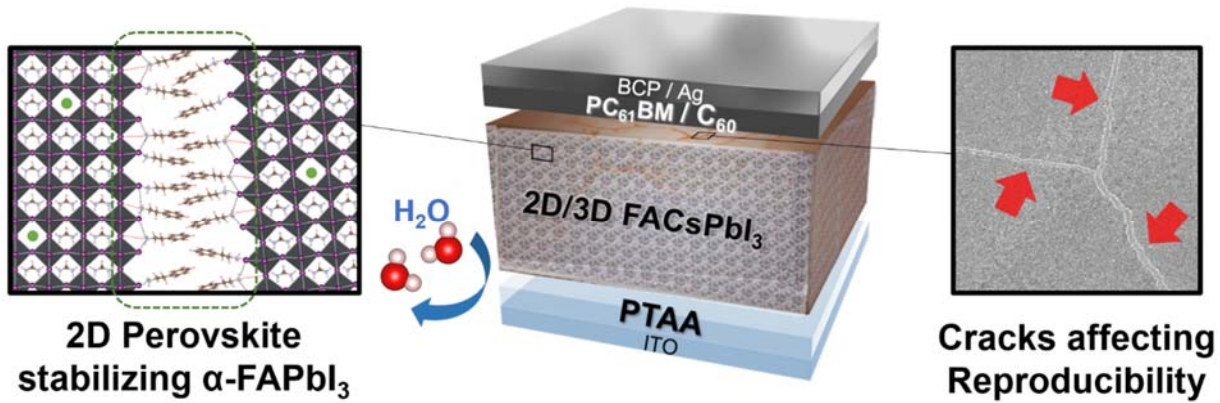
Supporting Information

Stable and Reproducible 2D/3D Formamidinium–Lead–Iodide Perovskite Solar Cells

Abhishek Thote[1‡], Il Jeon*[1‡], Jin-Wook Lee[2], Seungju Seo[1], Hao-Sheng Lin[1], Yang Yang[2],

Hirofumi Daiguji*[1], Shigeo Maruyama*[1,3], and Yutaka Matsuo*[1]

[1]Department of Mechanical Engineering, School of Engineering, The University of Tokyo, Tokyo

113-8656, Japan

[2]Department of Materials Science and Engineering and California Nano Systems Institute,

University of California, Los Angeles, CA 90095, United States

[3]Energy Nano Engineering Laboratory, National Institute of Advanced Industrial Science and

Technology (AIST), Ibaraki 305-8564, Japan

‡ These authors contributed equally.

I.J. E-mail: il.jeon@spc.oxon.org

H.D. E-mail: daiguji@thml.t.u-tokyo.ac.jp

S.M. E-mail: maruyama@photon.t.u-tokyo.ac.jp

Y.M. E-mail: matsuo@photon.t.u-tokyo.ac.jp
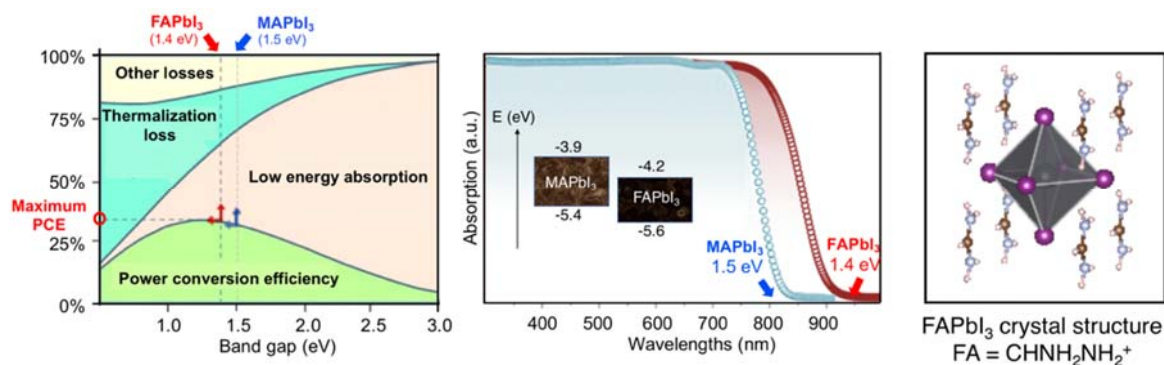
Figure S1. Graph depicting the relationship between the Shockley–Queisser limit and perovskite materials (left), illustration of UV-vis absorption spectra of MAPbI$_{33}$ and FAPbI$_3$ with their energy levels as an inset (middle), and 3D depiction of FAPbI$_3$ molecular crystallography.
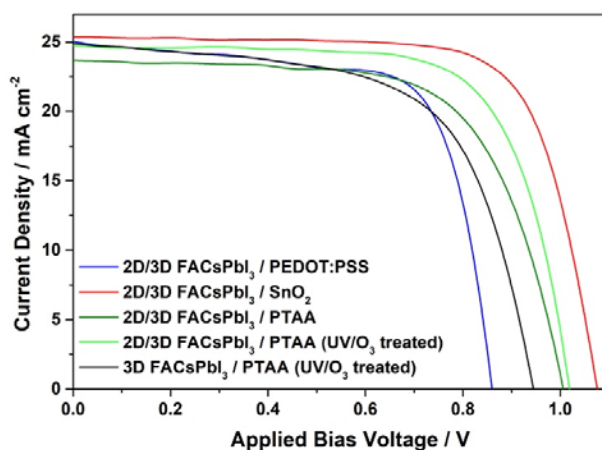
Figure S2. Forward bias J–V curves of inverted type PSCs on PEDOT:PSS (blue), PTAA (green), ozone-treated PTAA (light green); and a normal-type PSC on SnO$_2$ (red).

Table S1. Photovoltaic performance of inverted type PSCs with different annealing temperatures of the perovskite solution.

Temperatures (°C)	J_{SC} (mA cm^{-2})	V_{OC} (V)	FF	PCE (%)
55	23.2	0.80	0.67	12.9
75	24.1	0.82	0.66	13.0
95	24.2	0.85	0.66	13.6
105	23.8	0.72	0.66	11.4

Table S2. Photovoltaic performance of inverted type PSCs with different PTAA concentrations.

PTAA concentration (g ml^{-1})	J_{SC} (mA cm^{-2})	V_{OC} (V)	FF	PCE (%)
2	24.8	0.86	0.60	12.9
3	24.3	0.97	0.69	16.3
4	23.9	0.99	0.69	16.6
5	22.1	0.98	0.66	14.2

Table S3. Photovoltaic performance of inverted type PSCs with different ozone-treatment times on the PTAA layer.

UV/O$_3$ time (min)	J_{SC} (mA cm^{-2})	V_{OC} (V)	FF	PCE (%)
5	23.5	0.908	0.68	14.5
4	24.3	0.937	0.64	15.0
3	24.6	1.02	0.72	18.2
2	24.7	1.01	0.70	17.5
1	23.0	1.01	0.66	15.8
0	23.7	1.00	0.66	16.0
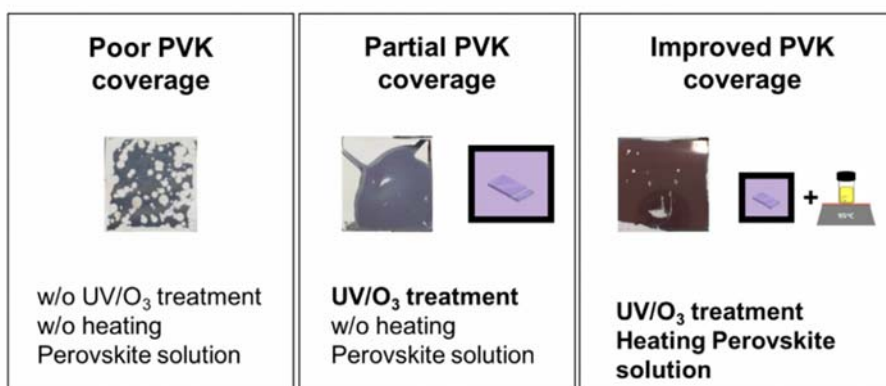
Figure S3. Pictures showing improvements in the perovskite (PVK) film coverage after ozone-treatment and heating.
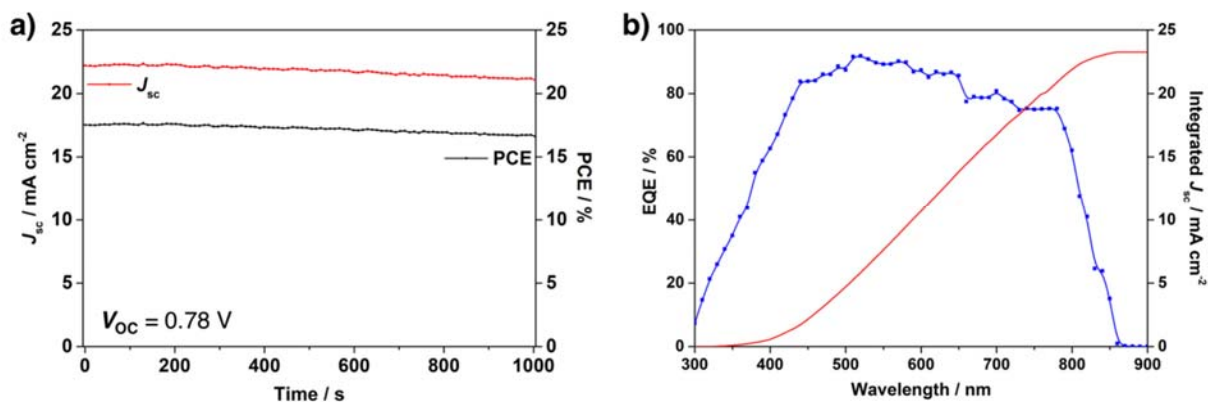
Figure S4. (a) MPPT data of the optimized inverted type 2D/3D FACsPbI$_3$-based PSC using PTAA. (b) External quantum efficiency of the same device with integrated J_{SC}.
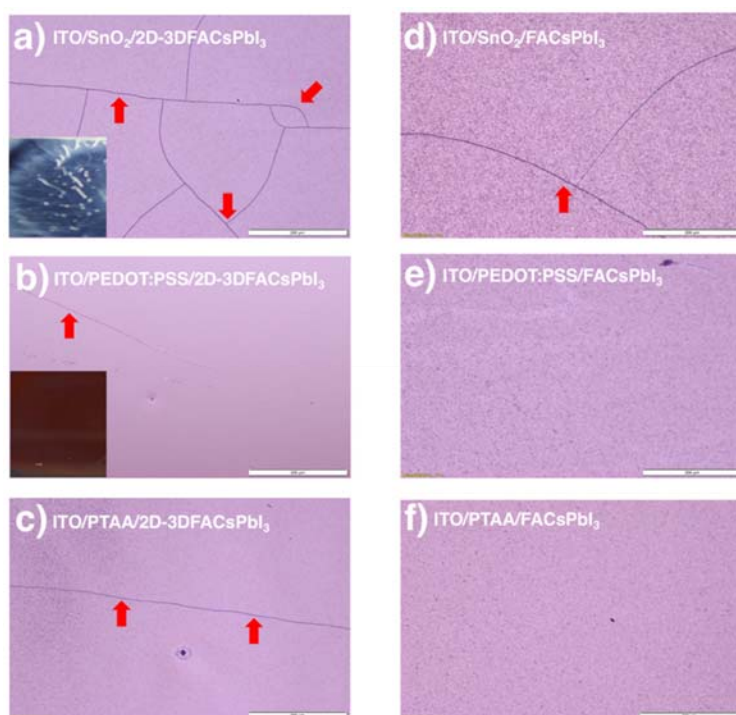
Figure S5. Optical microscopic images of 2D/3D FACsPbI$_3$ films on (a) SnO$_2$, (b) PEDOT:PSS (photographic images as insets), and (c) PTAA and FACsPbI$_3$ on (d) SnO$_2$, (e) PEDOT:PSS, and (f) PTAA.

Nano-indentation Test

The indentation hardness, elastic modulus, and Martens hardness were derived from the load displacement curves (**Figure S6**).[1] The indentation hardness is given by

$$H_{IT} = \frac{L_{max}}{A_p(h_c)} = \frac{L_{max}}{23.96 \times h_c^2},$$ (S1)

where A_p is the projected area of the indenter as a function of the contact depth h_c at the maximum load L_{max}. For a perfect Berkovich indenter, the projected area is given by $A_p = 23.96 \times h_c^2$. The contact depth is calculated from $h_c = h_{max} - \varepsilon(h_{max} - h_r)$, where h_{max} is the maximum depth and h_r is found as the crossing of the x-axis of a line originating from the top of the unloading curve with the slope of the tangent of the unloading curve (the contact stiffness $S = dL/dh$), and ε is the intercept factor. For a perfect Berkovich indenter, $\varepsilon = 0.75$. The elastic modulus is defined as follows:

$$E_{IT} = \frac{1-(v_s)^2}{\frac{1}{E_r} - \frac{1-(v_i)^2}{E_i}},$$ (S2)

where v_s and v_i are the Poisson's ratios of the specimen and the indenter, respectively. E_i is the elastic modulus of the indenter and E_r is the reduced modulus, which takes into account the induced elastic deformations in both the indenter and the specimen. The value of E_r is given as $E_r = \sqrt{\pi}/(2C\sqrt{A_p})$, where C is the contact compliance $C = dh/dL$. (The contact compliance is the reciprocal of the contact stiffness.) The Martens hardness is given by

$$HM = \frac{L}{A_s(h)} = \frac{L}{26.43 \times h^2} = \frac{L_{max}}{26.43 \times h_{max}^2}$$ (S3)

where L is the load and A_s is the contact area between the indenter and the specimen as a function of the displacement of the indenter h. For a perfect Berkovich indenter, the contact area is given by $A_s = 26.43 \times h^2$.
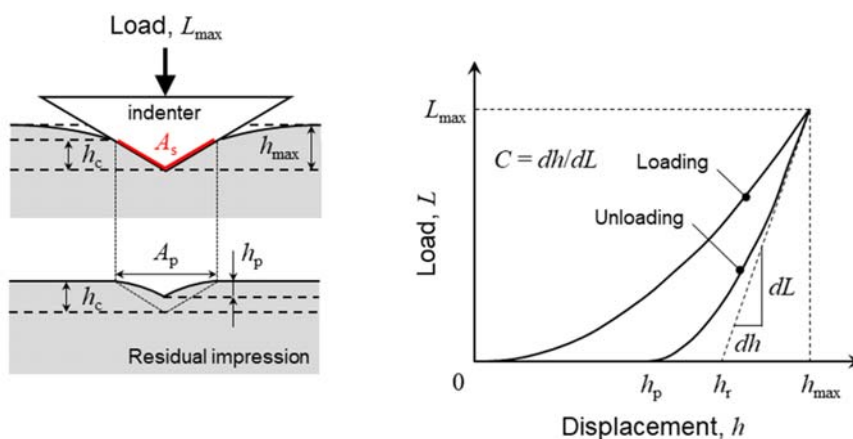
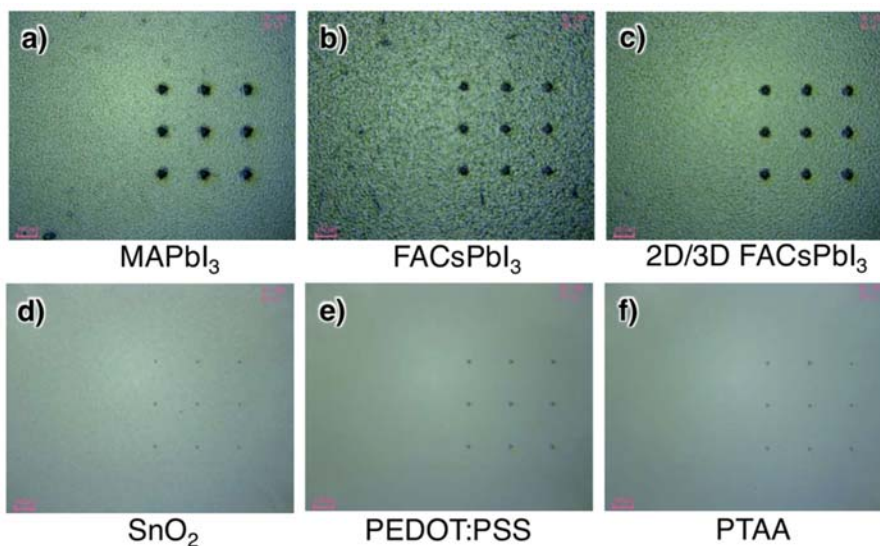**Figure S6**. Loading-unloading during nano-indentation test (left) and derived load-displacement curves (right).

Figure S7. Photographic images of the nano-indentation test on (a) MAPbI$_3$, (b) FACsPbI$_3$, (c) 2D/3D FACsPbI$_3$, (d) SnO$_2$, (e) PEDOT:PSS, and (f) PTAA.
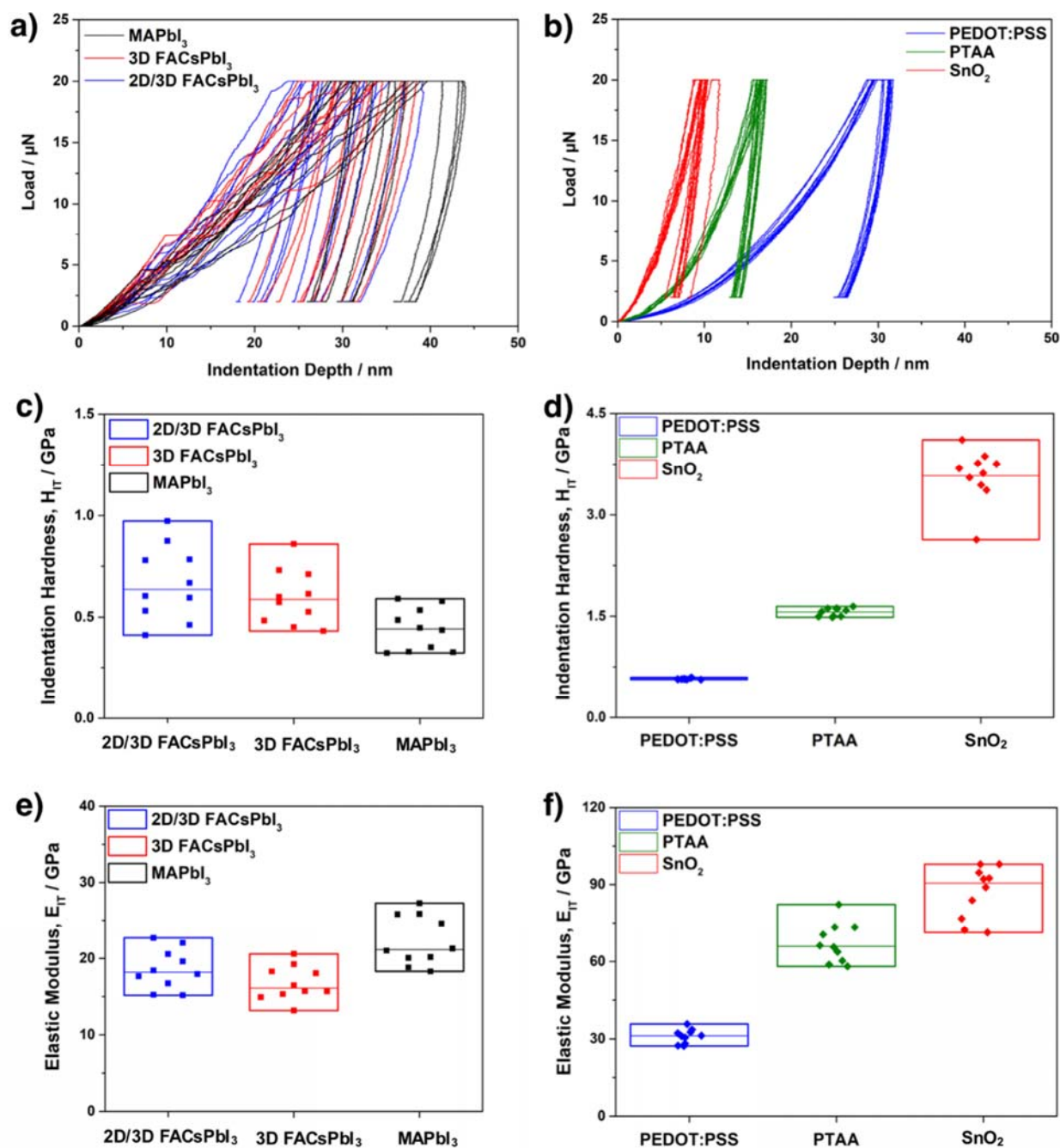
Figure S8. Load displacement curves of the nano-indentation test on a) the perovskite films and b) the sublayers. Indentation hardness plots of c) the perovskite films and d) the sublayers. Elastic modulus plots of e) the perovskite films and f) the sublayers.
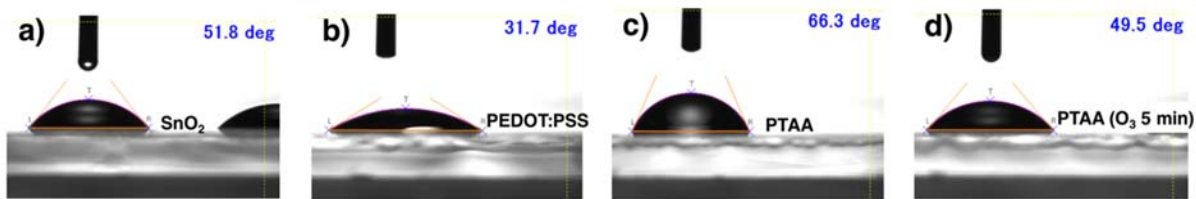
Figure S9. Water contact angles of (a) a SnO_2 film, (b) a PEDOT:PSS film, (c) a PTAA film, and (d) an ozone-treated PTAA film.
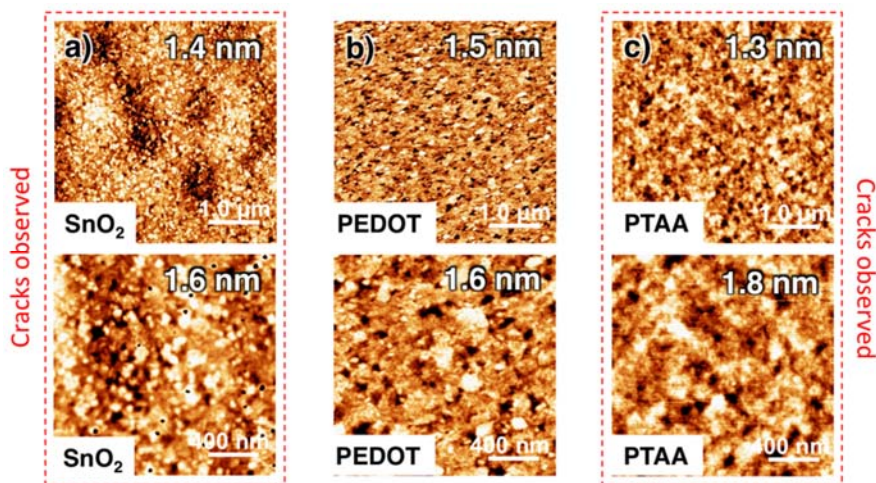
Figure S10. AFM images in 5 μm × 5 μm (above) and 2 μm × 2 μm (below) scales for (a) SnO_2 film, (b) PEDOT:PSS film, and (c) PTAA film with R_a values.
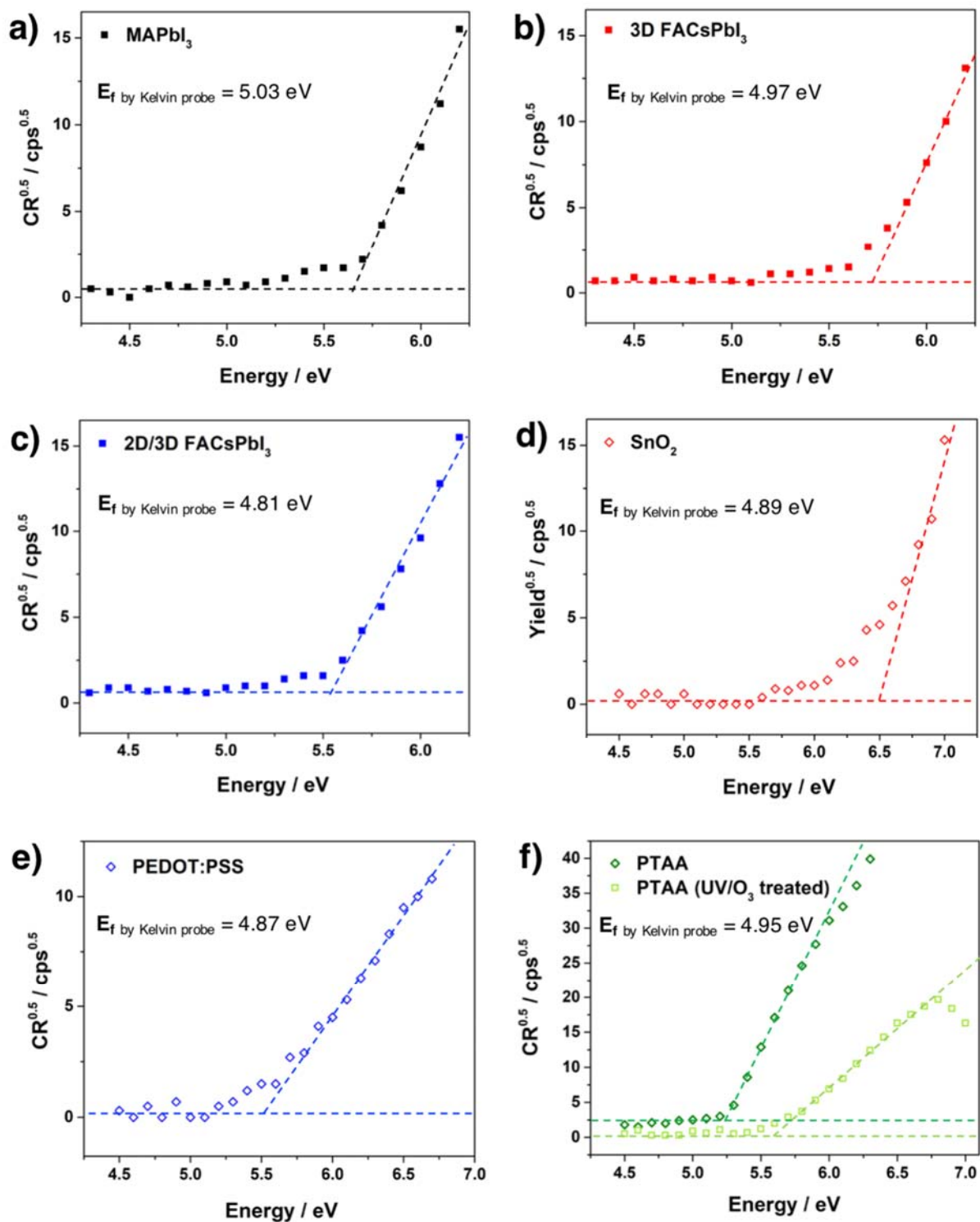
Figure S11. PYS data of (a) MAPbI₃, (b) 3D FACsPbI₃, (c) 2D/3D FACsPbI₃, (d) SnO₂, (e) PEDOT:PSS and (f) PTAA.
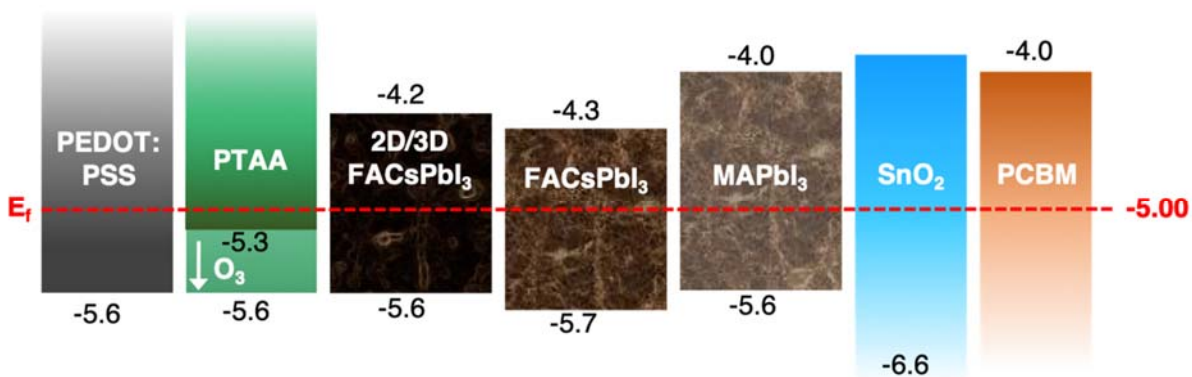
Figure S12. Energy level diagram of the films measured using PYS and the Kelvin probe.
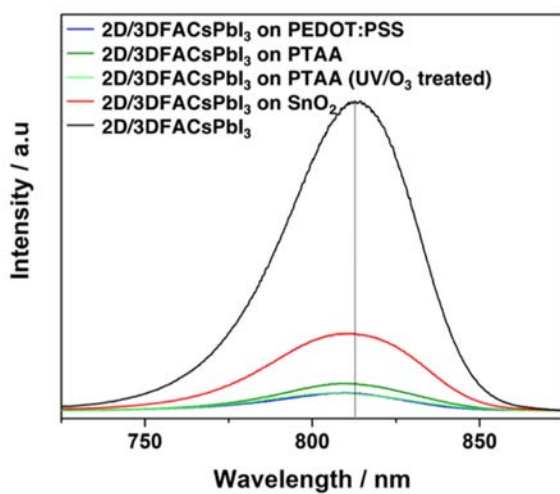
Figure S13. Photoluminescence data of 2D/3D FACsPbI₃ on various sublayers.

Figure S14. Pictures of the perovskite films on different sublayers degrading over 15 days.
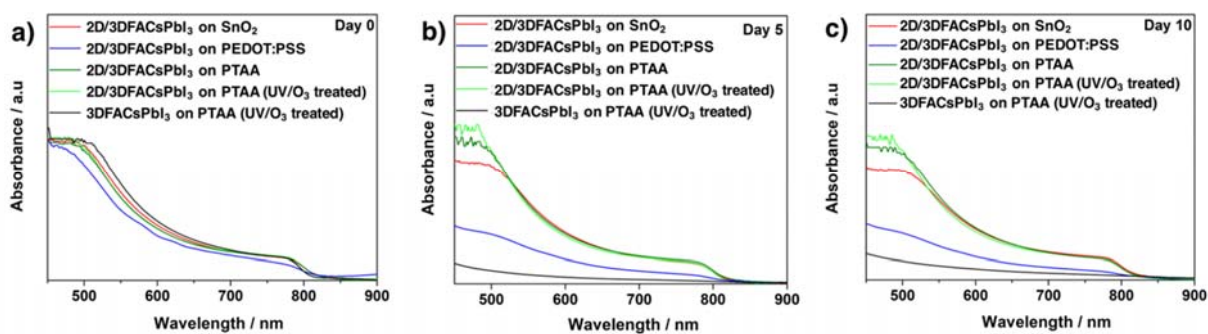
Figure S15. UV-vis absorption spectra of perovskite films on (a) Day 0 (b) Day 5 and (c) Day 10 on various sublayers (25 °C, 40% R.H).
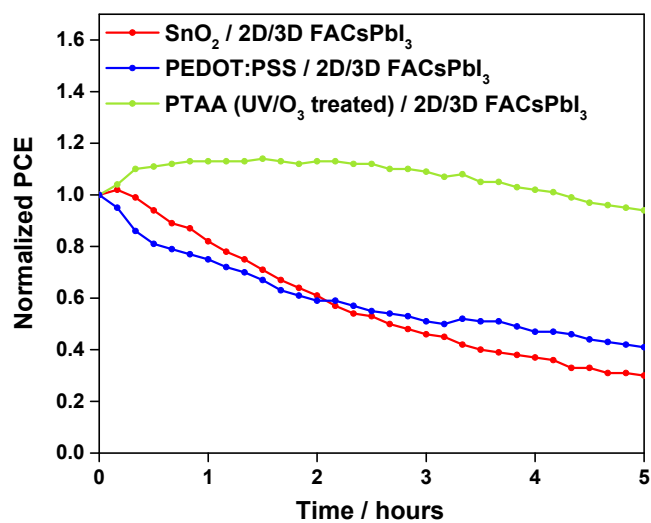
Figure S16. Stability test result of unencapsulated PSCs using a SnO$_2$ (red), PEDOT:PSS (blue) and UV/O3 treated PTAA (green) under constant illumination in air (20 °C, 40% R.H).
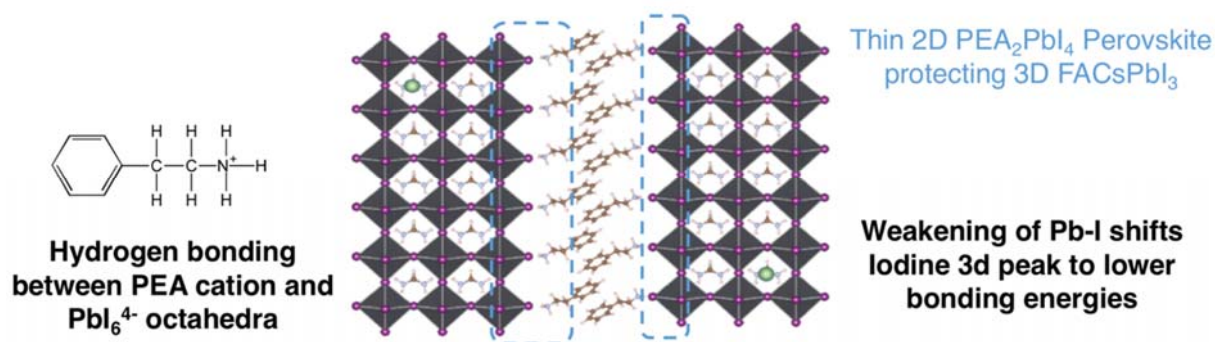

Figure S17. Illustration of interactions at the boundaries of 2D/3D FACsPbI$_3$.
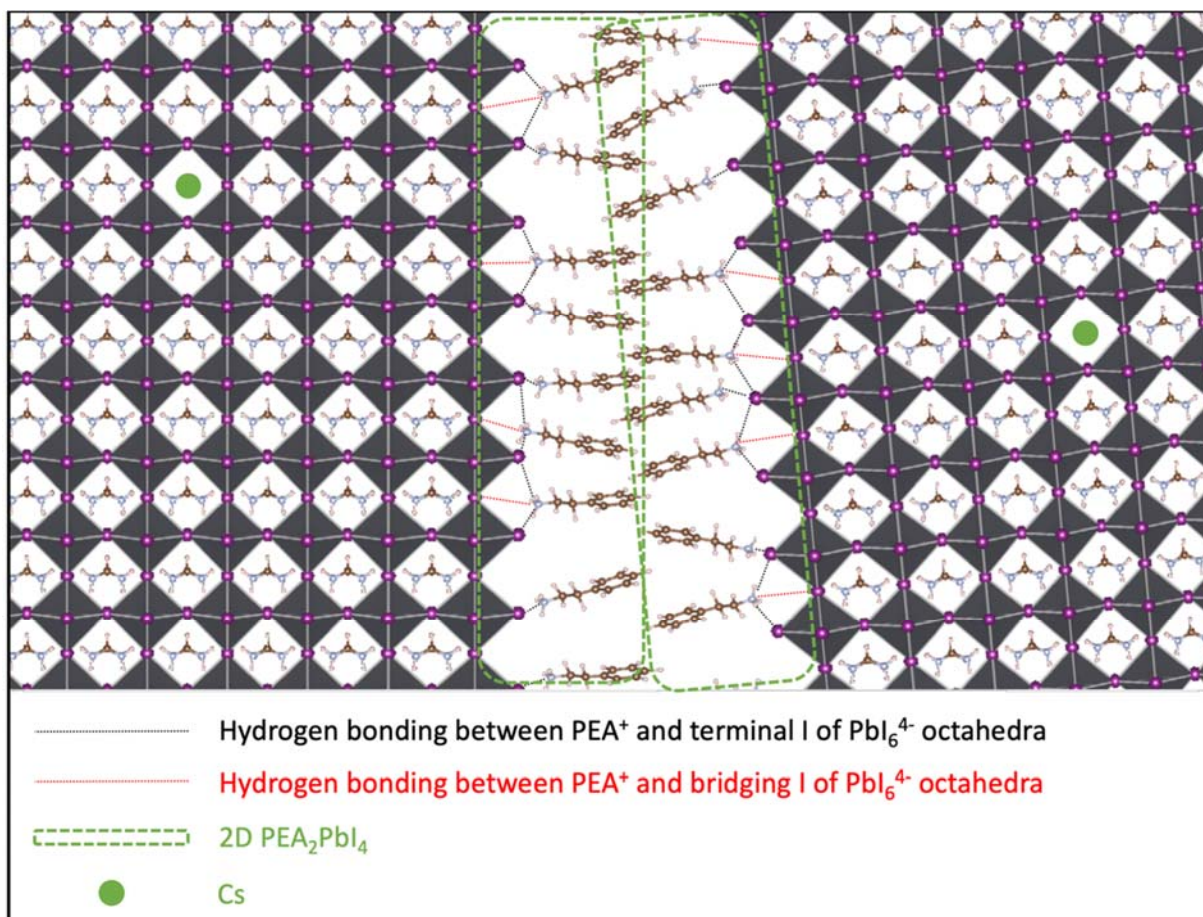
Figure S18. Illustration of interactions between molecules at the boundaries of 2D/3D FACsPbI$_3$.
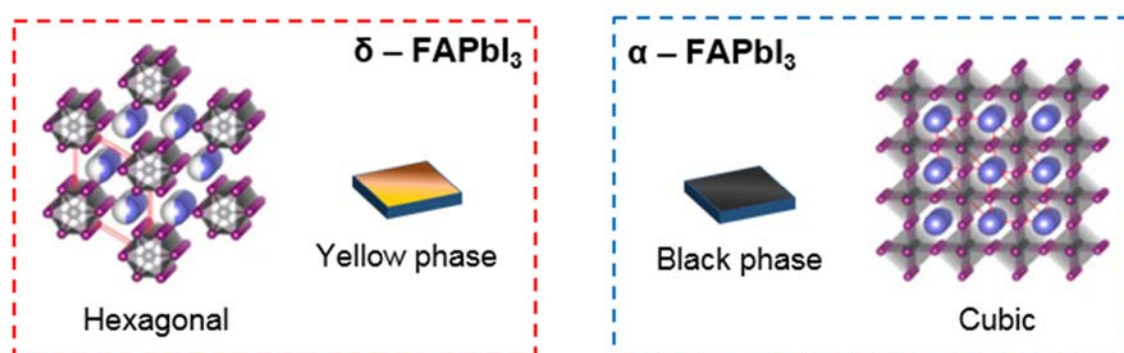

Figure S19. Illustration of δ-phase (left) and α-phase (right) formed by FAPbI$_3$ (modified images reproduced with permission from ref 50. Copyright © 2017, American Chemical Society)

REFERENCES

(1)   Metallic materials–Instrumented indentation test for hardness and materials parameters–
        Part 1: Test method. *ISO International Organization for Standardization* **2015**, *77.040.10*,
        ISO 14577-1.